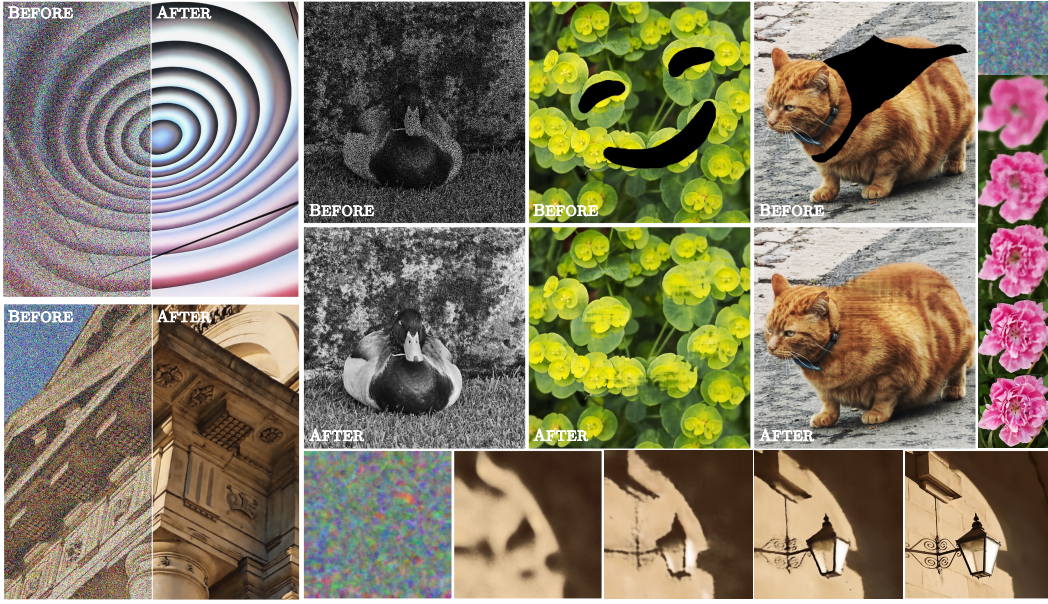


# Deep Spectral Prior

Yanqi Cheng<sup>1</sup> Tieyong Zeng<sup>2</sup> Pietro Lio<sup>1</sup> Carola-Bibiane Schönlieb<sup>1</sup>  
 Angelica I Aviles-Rivero<sup>3</sup>✉

<sup>1</sup> University of Cambridge <sup>2</sup> The Chinese University of Hong Kong <sup>3</sup> YMSC, Tsinghua University



## Abstract

We introduce Deep Spectral Prior (DSP), a new formulation of Deep Image Prior (DIP) that redefines image reconstruction as a frequency-domain alignment problem. Unlike traditional DIP, which relies on pixel-wise loss and early stopping to mitigate overfitting, DSP directly matches Fourier coefficients between the network output and observed measurements. This shift introduces an explicit inductive bias towards spectral coherence, aligning with the known frequency structure of images and the spectral bias of convolutional neural networks. We provide a rigorous theoretical framework demonstrating that DSP acts as an implicit spectral regulariser, suppressing high-frequency noise by design and eliminating the need for early stopping. Our analysis spans four core dimensions establishing smooth convergence dynamics, local stability, and favourable bias–variance tradeoffs. We further show that DSP naturally projects reconstructions onto a frequency-consistent manifold, enhancing interpretability and robustness. These theoretical guarantees are supported by empirical results across denoising, inpainting, and super-resolution tasks, where DSP consistently outperforms classical DIP and other unsupervised baselines.

# 1 Introduction

Inverse problems lie at the heart of image restoration and reconstruction, encompassing tasks such as denoising, inpainting, super-resolution, and deblurring. Traditionally approached through handcrafted priors and variational optimisation, these problems have seen a paradigm shift with the advent of deep learning, with single-image techniques effectively leverage data [10, 8, 7]. Among the most intriguing developments in this space is the Deep Image Prior (DIP) [34], which showed that the structure of an untrained convolutional neural network (CNN) alone can act as a powerful prior. By optimising a randomly initialised network to match a single degraded observation, DIP enables high-quality reconstructions—without requiring any training data. This surprising result has made DIP a widely adopted framework across diverse domains, including hyperspectral [27], microscopy [36, 47], compressed sensing [35], and medical imaging [12, 42, 2, 19, 18].

Despite its empirical success, DIP suffers from two key limitations that hinder its practical effectiveness. First, DIP is notoriously prone to overfitting. Due to the lack of explicit regularisation, the network can memorise noise or artifacts if optimisation proceeds too long, requiring ad hoc early stopping based on visual inspection [37]. Second, DIP’s pixel-wise reconstruction loss provides no explicit mechanism to control the frequency content or semantic structure of the recovered image. As a result, it tends to favor smooth, low-frequency components early in optimisation (due to spectral bias), while high-frequency details—such as texture or fine edges—are either fit too late or overfit entirely if optimisation proceeds unchecked [26, 34].

To mitigate these issues, recent work has explored two main directions [9, 16, 6, 46]. One line of research modifies the DIP architecture or optimisation dynamics—e.g., by freezing weights and optimising the input [32]. Another line of work augments DIP with explicit regularisers, such as Total Variation (TV) [30, 20] or Regularisation by Denoising (RED) [28, 24]. From the perspective of inverse problems, such double-prior formulations are theoretically beneficial, as additional constraints help mitigate the inherent ill-posedness. However, these approaches fundamentally alter the nature of DIP by introducing explicit handcrafted or learned priors, additional hyperparameters, and tuning requirements. They move away from DIP’s core appeal: solving inverse problems using only the implicit regularisation of a randomly-initialised network, without any external data or assumptions. Once explicit regularisation is introduced, it becomes unclear whether performance gains stem from the network’s inductive bias or the added constraint. As such, direct comparisons with these methods obscure the role of implicit regularisation alone in reconstruction performance. In contrast, our goal is to retain the original spirit of DIP while addressing its limitations from within the single-prior framework.

**Contributions.** We introduce **Deep Spectral Prior (DSP)**, a new unsupervised framework for solving inverse problems in imaging that operates directly in the frequency domain. In particular:

- A new spectral-domain formulation of that disentangles frequency content. We reformulate image reconstruction as direct optimisation over Fourier coefficients, allowing fine-grained control over frequency modes. Unlike DIP, DSP enables structured frequency modulation and corrects DIP’s spectral bias. DSP imposes a spectral inductive bias aligned with both the statistics of images and the known learning dynamics of convolutional networks.
- We establish the theoretical foundations of DSP and characterise its implicit regularisation:
  - We prove that DSP biases reconstruction toward low-frequency structure while attenuating high-frequency noise, eliminating the need for early stopping. This is formalised through Theorem A.1, which characterises frequency-dependent convergence of the reconstruction error.
  - We show that the DSP loss is continuously differentiable, locally Lipschitz, and supports stable descent under first-order optimisers (Theorem A.2). We further show that DSP exhibits spectrally ordered convergence aligned with the spectral bias of CNNs (Proposition A.1), explaining its robustness and stability across tasks.
  - We show that DSP implicitly projects reconstructions onto a frequency-consistent manifold (Proposition A.3), achieves a favourable bias–variance tradeoff in the Fourier domain (Proposition A.3), and suppresses high-frequency noise without explicit priors (Proposition A.3), explaining its stability and performance across diverse inverse problems.
- We evaluate DSP on several inverse problems, comparing against DIP, and recent deep unsupervised baselines. DSP consistently outperforms DIP across all tasks and images—often by significant margins. Given the widespread and enduring use of DIP as a general-purpose implicit prior, we

believe DSP opens a new line of research in frequency-domain implicit methods with similar long-term impact.

## 2 Methodology: Deep Spectral Prior

We introduce Deep Spectral Prior (DSP), a new formulation of Deep Image Prior (DIP) that shifts the reconstruction objective from pixel space to the frequency domain. While DIP minimises a pixel-wise loss, conflating frequency content and requiring early stopping, DSP directly matches Fourier coefficients, introducing a frequency-aware inductive bias. This leverages both the spectral structure of images and the spectral bias of CNNs, yielding sharper, more stable reconstructions without explicit regularisation. We show that this shift gives rise to distinct theoretical properties across four dimensions: regularisation, optimisation, geometry, and robustness.

### 2.1 From Pixels to Frequencies: Deep Spectral Prior

Let the observed degraded image be  $y = Ax + \epsilon$ , where  $A$  is a known degradation operator and  $\epsilon$  denotes additive noise. Let  $\hat{x}_\theta = f_\theta(z) \in \mathbb{R}^{H \times W}$  denote the output of a convolutional network with fixed random input  $z$ , and let  $\mathcal{F}(\cdot)$  denote the two-dimensional discrete Fourier transform (DFT).

Rather than minimising a spatial-domain loss, **Deep Spectral Prior** directly aligns Fourier coefficients via  $\mathcal{L}(\theta) := \|\mathcal{F}(A\hat{x}_\theta) - \mathcal{F}(y)\|_2^2$ . This reframes the objective from local pixel fidelity to global spectral coherence, reinforcing the natural low-frequency bias of images and CNNs. By decoupling signal from pixel-wise noise, DSP improves robustness and convergence. In the following, we show that DSP acts as an *implicit spectral regulariser*, aligned with both image statistics and network dynamics. We begin with a theoretical result that formalises how DSP naturally regularises reconstructions in the frequency domain. This reveals that DSP inherits the implicit spectral bias of CNNs but enhances it with a loss that prioritises low-frequency alignment.

**Definition 2.1. Deep Spectral Prior Loss.** *To incorporate inductive bias from the frequency domain, DSP modifies the reconstruction loss to operate in the Fourier domain. Specifically, the network parameters are optimised as:*

$$\theta^* = \arg \min_{\theta} \|\mathcal{F}(Af_\theta(z)) - \mathcal{F}(y)\|_2^2,$$

where  $\mathcal{F}$  denotes the (possibly non-normalised) discrete Fourier transform,  $A$  is the degradation operator, and  $y$  is the observed corrupted image. This retains the self-supervised nature of DIP by relying only on the observed measurement  $y$ , while leveraging frequency information to guide reconstruction.

### 2.2 Spectral Regularisation and Implicit Bias of Deep Spectral Prior

We now formalise how the frequency-domain loss in DSP implicitly regularises the reconstruction. The following theorem shows that, under mild assumptions, DSP preserves low-frequency structure while attenuating high-frequency noise—providing a natural form of spectral denoising. This reveals that DSP inherits the implicit spectral bias of CNNs but enhances it with a loss that prioritises low-frequency alignment.

**Theorem 2.1. (Spectral Regularisation in DSP).** *Let  $f_\theta : \mathbb{R}^d \rightarrow \mathbb{R}^n$  be a convolutional neural network with parameters  $\theta$ , and let  $z \in \mathbb{R}^d$  be a fixed random input. Let  $y \in \mathbb{R}^m$  be a corrupted observation of an unknown clean image  $x \in \mathbb{R}^n$ , with a known corruption operator  $\mathcal{A} : \mathbb{R}^n \rightarrow \mathbb{R}^m$ . Let  $\mathcal{F} : \mathbb{R}^m \rightarrow \mathbb{C}^m$  denote the discrete Fourier transform. Define the frequency loss:  $\mathcal{L}_{\text{DSP}}(\theta) := \|\mathcal{F}(\mathcal{A}f_\theta(z)) - \mathcal{F}(y)\|_2^2$ . Assume:*

1. *The network  $f_\theta$  is trained using a smooth optimiser (e.g., gradient descent or Adam with small learning rate);*
2. *The network exhibits spectral bias, i.e., for training time  $t$ ,*

$$\left\| \frac{\partial}{\partial t} \mathcal{F}(f_\theta(z))(\omega) \right\| \text{ decreases as } \|\omega\| \text{ increases};$$

3. The corruption noise  $\eta = y - \mathcal{A}x$  is high-frequency, i.e.,

$$|\mathcal{F}(\eta)(\omega)| \text{ is large for high } \|\omega\| \text{ and small for low } \|\omega\|.$$

Then the optimiser converges to  $\hat{\theta} = \arg \min_{\theta} \mathcal{L}_{\text{DSP}}(\theta)$  such that the reconstruction  $\hat{x} = f_{\hat{\theta}}(z)$  satisfies:

$$|\mathcal{F}(\mathcal{A}\hat{x})(\omega)| \approx |\mathcal{F}(y)(\omega)| \text{ for low } \|\omega\|, \quad \text{and} \quad |\mathcal{F}(\mathcal{A}\hat{x})(\omega)| < |\mathcal{F}(y)(\omega)| \text{ for high } \|\omega\|.$$

Hence, DSP suppresses high-frequency noise and does not require early stopping. (See proof in Appendix.)

To our knowledge, this is the first theoretical justification that using a Fourier magnitude loss (as in DSP) removes the need for early stopping in Deep Image Prior training. The result builds on spectral bias [26] properties but extends them with a formal optimisation perspective. Moreover, Theorem A.1 illustrates how DSP leverages both the spectral properties of images and the inherent frequency bias of neural networks. Low-frequency components, which dominate perceptual quality, are reconstructed accurately, while high-frequency noise—typically introduced by the degradation process—is suppressed. Crucially, this behaviour emerges *without* the need for early stopping, which is essential in classical DIP.

That is, Theorem A.1 establishes that the DSP loss, by prioritising low-frequency fidelity, inherently suppresses high-frequency noise—eliminating the need for early stopping, a crucial drawback in classical DIP. However, this result characterises the behaviour only at convergence. To gain a deeper understanding of how this behaviour emerges during training, we now turn to the optimisation trajectory of DSP. In particular, we ask: *How does the reconstruction evolve in the frequency domain over time?* The following proposition addresses this question by describing the frequency-wise convergence dynamics of the network output. It reveals that DSP not only converges to frequency-consistent reconstructions but does so in a spectrally ordered fashion, aligning with the spectral bias of convolutional networks.

**Proposition 2.1 (Gradient Dynamics in Frequency Space).** *Consider the frequency-domain loss  $\mathcal{L}_{\text{DSP}}(\theta) := \|\mathcal{F}(\mathcal{A}f_{\theta}(z)) - \mathcal{F}(y)\|_2^2$ . Then, when the parameters  $\theta$  are updated by a smooth optimisation algorithm with small learning rate, the iterates  $\{\theta_t\}$  yield reconstructions  $u_t := \mathcal{A}f_{\theta_t}(z)$  such that*

$$\mathcal{F}(u_t) \rightarrow \mathcal{F}(y) \quad \text{in } \mathbb{C}^m.$$

*Moreover, if the network  $f_{\theta}$  exhibits spectral bias, then the components of  $\mathcal{F}(u_t)$  at low spatial frequencies converge faster than those at high frequencies. (See proof in Appendix.)*

### 2.3 Optimisation Properties of Deep Spectral Prior

Having shown that DSP introduces a desirable regularisation mechanism, we now examine its optimisation properties. Specifically, we verify that the frequency loss is smooth, locally stable, and conducive to convergence under standard first-order methods. This theoretical part explains why DSP is compatible with common optimisers like Adam and why its convergence dynamics remain stable across diverse inverse tasks.

**Theorem 2.2 (Smoothness and Local Stability of our Frequency Loss).** *Let  $f_{\theta} : \mathbb{R}^d \rightarrow \mathbb{R}^n$  be a neural network that is continuously differentiable with respect to parameters  $\theta \in \mathbb{R}^p$ . Let  $\mathcal{A} : \mathbb{R}^n \rightarrow \mathbb{R}^m$  be a fixed linear corruption operator, and let  $\mathcal{F} : \mathbb{R}^m \rightarrow \mathbb{C}^m$  denote the discrete Fourier transform (DFT). For a fixed input  $z \in \mathbb{R}^d$  and observed corrupted image  $y \in \mathbb{R}^m$ , define the DSP frequency loss as:  $\mathcal{L}_{\text{DSP}}(\theta) := \|\mathcal{F}(\mathcal{A}f_{\theta}(z)) - \mathcal{F}(y)\|_2^2$ . It follows that:*

1.  $\mathcal{L}_{\text{freq}}$  is continuously differentiable with respect to  $\theta$ ;
2.  $\mathcal{L}_{\text{freq}}$  is locally Lipschitz in  $\theta$ ;
3. Any local minimum  $\theta^*$  satisfies the first-order optimality condition  $\nabla_{\theta} \mathcal{L}_{\text{freq}}(\theta^*) = 0$ ;
4. In a neighborhood of any stationary point  $\theta^*$ , gradient-based optimisation (e.g., gradient descent or Adam with sufficiently small step size) yields descent in the frequency domain,

$$\mathcal{L}_{\text{freq}}(\theta_{t+1}) \leq \mathcal{L}_{\text{freq}}(\theta_t),$$

for all  $t$  sufficiently large.

(See proof in Appendix.)

To solidify the theoretical foundation of DSP, it is critical to understand how frequency-domain objectives relate to their spatial-domain counterparts. The following result establishes that, under the unitary Fourier transform, minimising the DSP loss with complex-valued frequency alignment is strictly equivalent to minimising the traditional pixel-wise loss. This equivalence is not merely cosmetic: *it guarantees that the shift to the frequency domain does not alter the optimisation landscape*, but rather recasts it in a basis aligned with the spectral properties of images. In doing so, DSP inherits the guarantees of pixel-space reconstruction while gaining interpretability, robustness, and inductive alignment with convolutional architectures.

**Corollary 2.1 (Equivalence of Deep Spectral Prior Loss and Pixel-Space Error).** *Let  $x, \hat{x} \in \mathbb{R}^m$ , and let  $\mathcal{F} : \mathbb{R}^m \rightarrow \mathbb{C}^m$  denote the unitary discrete Fourier transform. Then:*

$$\|x - \hat{x}\|_2^2 = \|\mathcal{F}(x) - \mathcal{F}(\hat{x})\|_2^2.$$

*In particular, for any neural network output  $f_\theta(z)$  and measurement  $y$ , the complex-valued frequency-domain loss  $\mathcal{L}_{\text{DSP}}(\theta) := \|\mathcal{F}(\mathcal{A}f_\theta(z)) - \mathcal{F}(y)\|_2^2$  is exactly equal to the pixel-space reconstruction error  $\|f_\theta(z) - y\|_2^2$ . Thus, minimising  $\mathcal{L}_{\text{freq}}$  guarantees pixel-accurate recovery. (See proof in Appendix.)*

These properties guarantee that DSP remains compatible with standard deep learning practices and optimisers, while extending the functional landscape with frequency-aligned descent.

## 2.4 Spectral Geometry and Signal Structure

To further understand the effect of DSP on reconstruction quality, we analyse the bias–variance tradeoff in the frequency domain. This classical decomposition provides a quantitative lens on how DSP balances signal fidelity and robustness. In particular, we are interested in how frequency alignment affects the distribution of bias and variance across the spectrum. The following proposition formalises this decomposition, revealing how spectral bias in convolutional networks interacts with the DSP objective.

**Proposition 2.2 (Frequency-Domain Bias–Variance Tradeoff).** *Let  $\hat{x}_\theta$  be the network output trained to minimise the DSP loss  $\mathcal{L}(\theta) := \|\mathcal{F}(\mathcal{A}f_\theta(z)) - \mathcal{F}(y)\|_2^2$ . Then the expected error at convergence in the Fourier domain decomposes as*

$$\mathbb{E} \left[ \|\mathcal{F}(\hat{x}_\theta) - \mathcal{F}(x)\|_2^2 \right] = \underbrace{\|\mathbb{E}[\mathcal{F}(\hat{x}_\theta)] - \mathcal{F}(x)\|_2^2}_{\text{Bias}^2} + \underbrace{\mathbb{E} \left[ \|\mathcal{F}(\hat{x}_\theta) - \mathbb{E}[\mathcal{F}(\hat{x}_\theta)]\|_2^2 \right]}_{\text{Variance}}.$$

*Due to the spectral bias of convolutional networks, the bias term decays faster at low frequencies, while the variance remains higher in high-frequency components—resulting in implicit regularisation through spectral ordering. (See proof in Appendix.)*

This result clarifies the regularisation mechanism underlying DSP. Due to the spectral bias of neural networks, low-frequency components are fitted more consistently across different training runs, resulting in lower variance and faster convergence. Conversely, high-frequency components exhibit greater variance and are less stable, especially in the presence of noise. Crucially, the frequency-domain loss implicitly reflects this structure: although the loss penalises all frequency components equally in form, the network’s inductive bias causes the optimisation to prioritise smoother, low-frequency solutions. As a result, DSP achieves a favourable bias–variance profile without requiring explicit filtering or handcrafted priors. This behaviour contrasts sharply with classical DIP, where the pixel-space loss treats all spatial details equally, often leading to overfitting unless training is manually stopped. DSP, in contrast, exhibits natural spectral regularisation driven by both the loss and the optimiser’s dynamics.

While the previous bias–variance analysis quantifies how DSP balances expressivity and stability across frequency bands, we now shift to a geometric interpretation. Specifically, we ask: what set of signals does DSP consider valid reconstructions? The frequency-domain loss defines an implicit constraint: reconstructed images must match the observed measurement in the Fourier domain. This constraint naturally induces a manifold of frequency-consistent candidates. The following proposition formalises this idea, showing that DSP can be viewed as projecting the network output onto this manifold—thus ensuring spectral fidelity without requiring explicit supervision or regularisation.

**Proposition 2.3 (Implicit Projection onto the Frequency Consistency Manifold).** *Let  $f_\theta(z) \in \mathbb{R}^n$  denote the network output, and let  $\mathcal{A} \in \mathbb{R}^{m \times n}$  be a linear degradation operator. Define the frequency consistency manifold:*

$$\mathcal{M}_y := \{x \in \mathbb{R}^n : \mathcal{F}(\mathcal{A}x) = \mathcal{F}(y)\}.$$

*Then, at convergence, the DSP optimisation seeks a point  $\hat{x}_\theta$  satisfying:*

$$\hat{x}_\theta \approx \arg \min_{x \in \mathcal{M}_y} \|x - f_\theta(z_0)\|^2,$$

*where  $z_0$  is the fixed network input. That is, DSP approximates a projection of the unconstrained network output onto the frequency-consistent manifold  $\mathcal{M}_y$ . (See proof in Appendix.)*

This proposition offers a powerful geometric lens through which to interpret DSP. Rather than merely fitting data in an unconstrained optimisation landscape, DSP implicitly restricts solutions to lie on a low-dimensional manifold defined by spectral consistency with the measurement. This mechanism ensures that reconstructions preserve the frequency characteristics of the observed data while filtering out artefacts that violate this constraint. Importantly, this projection is implicit—it arises naturally from the optimisation dynamics, without requiring handcrafted priors or external supervision. By aligning the network’s output with a well-structured manifold, DSP stabilises the reconstruction process and improves generalisation across inverse problems. This interpretation also highlights how DSP turns frequency alignment into a form of data-driven constraint enforcement, distinguishing it fundamentally from pixel-space DIP which lacks such an explicit geometric prior.

A critical vulnerability of classical DIP is its tendency to overfit noise, especially when the corruption involves high-frequency perturbations. This is a direct consequence of its pixel-space loss, which treats all frequencies uniformly. In contrast, DSP exhibits a form of inherent robustness to such noise—without requiring explicit denoising modules or handcrafted priors. The next formalise this observation: under the spectral bias of deep convolutional networks, DSP naturally filters out high-frequency components of the noise and prioritises signal recovery in low-frequency bands. This explains why DSP maintains reconstruction quality even in challenging noisy regimes.

**Proposition 2.4 (Stability to High-Frequency Noise).** *Let  $y = \mathcal{A}x + \eta$ , where  $\eta \in \mathbb{R}^m$  is additive noise. Let  $\mathcal{F}$  denote the discrete Fourier transform, and suppose  $\eta$  is supported primarily in high-frequency bands. Consider the DSP loss:  $\mathcal{L}(\theta) := \|\mathcal{F}(\mathcal{A}f_\theta(z)) - \mathcal{F}(y)\|_2^2$ . Then, under spectral bias of  $f_\theta$ , the optimisation trajectory satisfies:*

$$\|\mathcal{F}(\mathcal{A}f_\theta(z)) - \mathcal{F}(x)\|_2^2 \leq \|\mathcal{F}(\eta_{<k})\|_2^2 + \mathcal{O}(t^{-\alpha}),$$

*where  $\eta_{<k}$  is the projection of  $\eta$  onto low-frequency components,  $t$  is the iteration index, and  $\alpha > 0$  is a constant determined by network architecture and depth. (See proof in Appendix.)*

This result confirms that DSP acts as a spectral filter during optimisation, concentrating its fitting capacity on the most informative frequency bands. Since high-frequency noise typically dominates the tail of the spectrum, its effect on the loss diminishes over time. The bound demonstrates that reconstruction error is ultimately governed by the low-frequency content of the noise, which tends to be minimal in natural settings. Practically, this means DSP avoids the need for early stopping, denoising pre-processing, or post-hoc regularisation. The network’s own training dynamics, when using the frequency loss, yield an implicit denoising mechanism.

### 3 Experimental Results

We evaluate DSP on blind denoising, restoration, super-resolution, and inpainting tasks. Our main goal is to benchmark against DIP as the foundational implicit prior, while also comparing to recent strong unsupervised and task-specific SOTA methods. DSP is proposed with the goal of not to beat all SOTA unsupervised techniques but to introduce a new direction for frequency-domain implicit models. We report PSNR and visual results (with zoom-in views) on standard benchmarks [23, 45, 14, 22, 43], using the same iteration schedule for DIP and DSP. All experiments run on a Tesla T4 GPU (15GB RAM).

**Blind Denoising.** In the blind denoising task, the forward measurement operator is the identity operator. We compare the denoising performance (measured in PSNR, dB) of our proposed DSP method with several established unsupervised approaches, including DIP [34], CBM3D [17], Noise2Self [3],

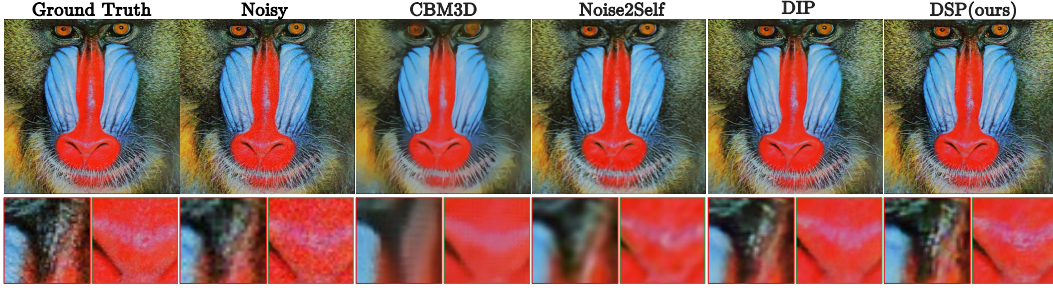


Figure 1: Visual comparison of blind denoising on the “Baboon” image. DSP (ours) is compared vs. unsupervised baselines, with zoomed-in views highlighting fine details preservation.

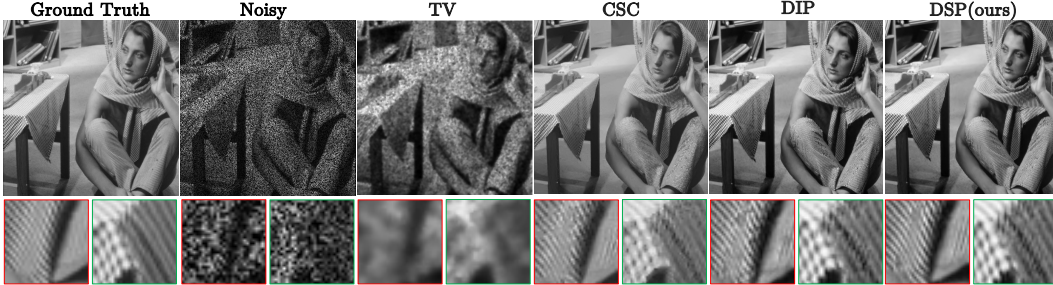


Figure 2: Restoration results on the “Barbara” image with heavy noise. DSP (ours) better preserves structured textures (e.g., fabric) compared to DIP, TV, and CSC, as shown in the zoomed-in regions.

Wavelet-based shrinkage [5], Total Variation (TV) denoising [4, 11], WIRE [31], and DS-N2N [1], across a variety of test images. As shown in Table 1, DSP achieves notable improvements over the baselines, particularly on fine-textured or complex regions such as “Plane” and “Brick Wall,” with gains of +1.69 dB and +1.53 dB over DIP, respectively. This suggests that DIP tends to overfit to noise or overly smooth detailed textures, whereas DSP better preserves structural details. Visual comparisons in Figure 1 further confirm these findings: DSP delivers cleaner reconstructions with enhanced texture fidelity, avoiding the patchy artefacts commonly observed in Noise2Self and the grid-like behaviour and over-smoothing typical of CBM3D in highly structured regions.

**Image Restoration.** In the image restoration task, a Bernoulli mask is applied as the forward measurement operator.

We compare our DSP method against baselines including DIP, and Convolutional Sparse Coding (CSC) [39] implemented with [40, 41]. As shown in Table 2, DSP consistently outperforms these methods. For example, on the “Barbara” image, which contains fine patterns and directional textures, DSP yields a higher PSNR than both DIP and TV, indicating better preservation of structured detail. Qualitative comparisons in Figure 2 further reveal that DSP reconstructs finer textures and edges more faithfully, whereas TV introduce artefacts in regions, CSC tend to produce over-smoothed results and DIP kept masked artifact with non smoothed edge features. These results highlight the capability of DSP to recover complex structures even under aggressive masking.

**Super Resolution.** For the super resolution task, the forward measurement operator corresponds to downsampling with fixed scaling factors. We compare our proposed DSP method with a range of both unsupervised and supervised baselines. The unsupervised group includes DIP [34], Total Variation (TV) [30], and Bicubic upsampling, while the supervised group comprises LapSRN[33], ResShift [44], SinSR [38] and ASID [25]. Since supervised methods are trained for fixed resolutions, only the officially available  $\times 4$  upscaling is evaluated. As supervised methods are trained for fixed resolutions, only the officially available  $\times 4$  results are reported. In contrast, DSP operates at arbitrary scales without any task-specific pretraining. As shown in Table 3, DSP consistently achieves the highest PSNR across all test images in both  $\times 4$  and  $\times 8$  settings among unsupervised methods. Notably, on the “Bird” image, DSP attains 30.27dB, outperforming DIP by over 1dB and even surpassing some supervised baselines such as SinSR and ResShift. Figure 3 offers a visual comparison on the “Zebra” image at  $\times 8$  upscaling. While supervised methods tend to produce smoother outputs, they often oversimplify textures due to reliance on generic learned priors. In

Table 1: Performance comparison (PSNR in dB) across unsupervised denoising methods (DIP, DSP, CBM3D, Noise2Self, Wavelet, Total Variation (TV), TV with split Bregman, WIRE and DS-N2N) on various images. Best values per image are highlighted in bold.

METHOD		Glass Roof	Orange Building	Brick Wall	Brick Building	Baboon	Monarch	Plane
Wavelet [5]	2000	21.37	26.54	24.76	22.19	22.16	28.91	28.45
TV [4]	2004	23.90	23.55	23.90	23.40	23.29	25.04	28.70
CBM3D [17]	2012	19.73	21.95	20.57	19.86	20.77	26.28	27.29
TV Bregman [11]	2012	17.45	22.70	21.29	18.58	19.53	23.26	24.28
DIP [34]	2018	24.26	27.65	24.27	22.95	22.77	30.99	28.83
Noise2Self [3]	2019	22.81	25.19	23.81	21.94	21.31	28.92	28.64
WIRE [31]	2023	19.92	25.41	22.93	20.35	21.57	29.22	29.64
DS-N2N [1]	2025	25.45	27.96	25.77	23.56	23.36	30.65	30.40
DSP (ours)	2025	<b>25.59</b>	<b>28.50</b>	<b>25.80</b>	<b>23.85</b>	<b>23.59</b>	<b>31.13</b>	<b>30.52</b>

Table 2: Performance comparison (PSNR in dB) across learned methods (CSC, DIP, DSP (ours)) on various images in Set12, with restoration tasks. Best values per image are highlighted in bold.

METHOD		Photo	House	Pepper	Starfish	Parrot	Man	Barbara
CSC [39]	2016	28.22	33.68	28.22	28.88	28.02	31.64	29.18
DIP [34]	2018	29.61	37.22	32.68	32.55	29.49	31.83	30.97
DSP (ours)	2025	<b>29.74</b>	<b>38.05</b>	<b>32.81</b>	<b>32.95</b>	<b>29.60</b>	<b>32.29</b>	<b>32.33</b>

Table 3: PSNR (dB) comparison across super-resolution methods (Bicubic, DIP, TV, LapSRN, ResShift, SinSR (with single step and 15 steps in [38]), and ASID with our proposed DSP on various test images. Best values for both supervised and unsupervised groups are highlighted in bold.

METHOD			Zebra		PPT		Flower		Comic		Bird	
			×4	×8	×4	×8	×4	×8	×4	×8	×4	×8
Unsup	Bicubic	–	23.10	18.55	20.31	17.17	23.76	20.52	20.20	17.77	28.44	23.30
	TV [30]	1992	23.51	18.68	20.51	17.32	23.99	20.66	20.32	17.84	28.75	23.67
	DIP [34]	2018	23.83	19.55	22.47	18.72	24.25	21.31	20.75	18.44	29.13	24.94
	DSP (ours)	2025	<b>24.31</b>	<b>19.68</b>	<b>22.99</b>	<b>18.84</b>	<b>24.57</b>	<b>21.41</b>	<b>20.90</b>	<b>18.48</b>	<b>30.27</b>	<b>25.04</b>
Sup	LapSRN [33]	2017	24.71	–	<b>24.26</b>	–	<b>26.08</b>	–	<b>21.49</b>	–	31.17	–
	ResShift [44]	2023	<b>25.03</b>	–	23.43	–	23.52	–	20.86	–	30.00	–
	SinSR [38]	2024	21.51	–	22.22	–	22.43	–	18.62	–	26.55	–
	SinSR 15	2024	21.67	–	22.10	–	22.28	–	19.09	–	26.75	–
	ASID [25]	2025	18.90	–	22.59	–	23.48	–	18.90	–	<b>32.59</b>	–

Table 4: Performance comparison across supervised methods (GLCIC and Prefpaint) and unsupervised methods (DIP and DSP (ours)) on inpainting tasks. Best values per image are highlighted.

METHOD			Vase	Street	Face	Beach	Shore	Glider	Backstreet	Library
Unsup	DIP [34]	2018	28.32	22.18	22.91	19.89	29.43	29.46	23.85	19.06
	DSP (ours)	2025	<b>29.44</b>	<b>22.63</b>	<b>23.52</b>	<b>20.06</b>	<b>31.27</b>	<b>29.96</b>	<b>26.34</b>	<b>19.37</b>
Sup	GLCIC [15]	2017	<b>29.51</b>	18.26	19.49	<b>20.15</b>	<b>31.12</b>	<b>30.39</b>	<b>26.77</b>	<b>18.88</b>
	Prefpaint [21]	2024	22.74	<b>23.21</b>	<b>25.43</b>	19.85	27.68	27.40	23.04	16.80

contrast, DSP better preserves fine structures such as the zebra’s stripes and background foliage, showing sharper detail and fewer artefacts than DIP. These results highlight DSP’s ability to recover image-specific features and fine textures in a single-shot, unsupervised setting—making it a flexible and robust approach for real-world super resolution tasks.

**Inpainting.** We evaluate DSP on the inpainting task using a range of unsupervised and supervised baselines. The unsupervised methods include DIP [34], while the supervised methods are UNet [30], ResNet [29, 13], GLCIC [15] and Prefpaint [21]. As shown in Table 4, DSP outperforms DIP across all test images, with consistent PSNR improvements. On several images such as “Shore” and “Library”, DSP even surpasses supervised methods, which confirm that DSP effectively leverages image-specific structures without requiring external training data. Qualitative results on the “Library” image are shown in Figure 4. DIP and ResNet produce dark twisted regions where the mask is present,

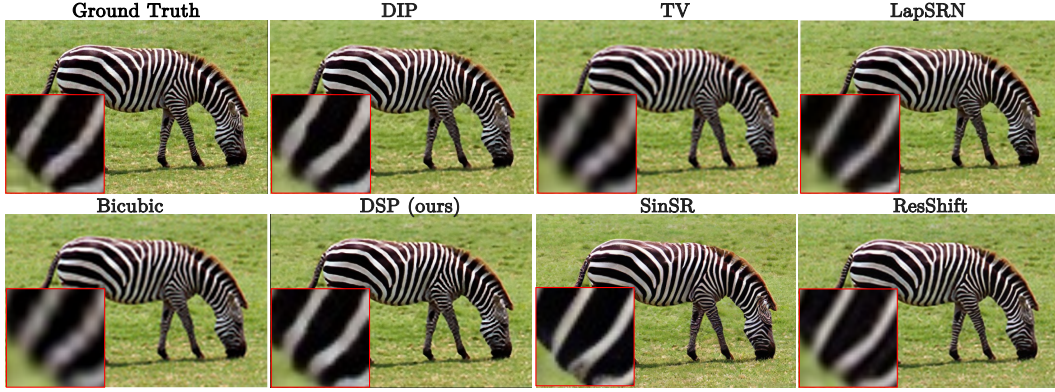


Figure 3: Comparison of super resolution task with  $4\times$  upscale on the “Zebra” image among Bicubic, TV, DIP, and the supervised methods (LapSRN, ResShift, and SinSR) with our proposed DSP.

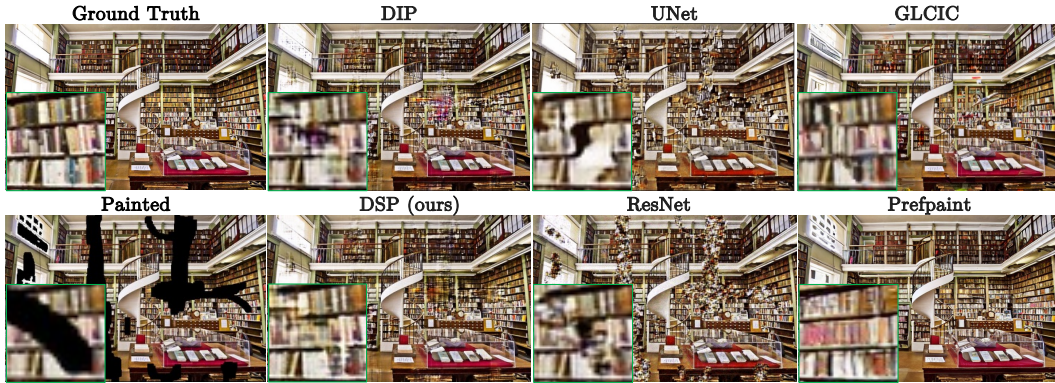


Figure 4: The visualisation comparison of inpainting task with on the “Library” image among DIP, UNet, ResNet, and GLCIC, Prepaint, and our proposed DSP.



Figure 5: The progression over iterations of the zoomed in of blind denoising task on the “Plane” image, with its Peak Signal-to-Noise Ratio (PSNR) of DIP and DSP (ours) methods.

indicating unstable reconstructions in under-constrained areas. UNet offers smoother outputs but fails to recover semantically plausible structures. GLCIC, a GAN-based method, introduces edge artefacts near mask boundaries, likely due to adversarial limitations. Although Prepaint yields clean and realistic completions, it diverges from the ground truth content, aligning instead with learned aesthetic preferences. In contrast, DSP generates visually coherent and structurally faithful reconstructions, striking a strong balance between realism and fidelity, despite operating entirely without supervision or pretrained models.

**Early Stopping Analysis.** We analyse the iterative progression of DIP and DSP on the “Plane” image from the blind denoising task, as visualised in Figure 5. DIP reaches its peak PSNR around 1800 iterations but then quickly dropped to 28.83 dB by iteration 3000 due to overfitting. In contrast, DSP improves steadily throughout optimisation, reaching 30.52 dB at 3000 iterations. The visual comparison shows that DSP produces increasingly cleaner and structurally consistent reconstructions, while DIP begins to introduce artefacts after its peak. This highlights DSP’s stability and robustness across iterations, especially in the absence of manual early stopping.

## 4 Conclusion

We introduced **Deep Spectral Prior** (DSP), a frequency-domain formulation for unsupervised image reconstruction. By shifting the optimisation objective from pixel space to the Fourier domain, DSP imposes an implicit spectral prior aligned with image statistics and the spectral bias of CNNs. This leads to sharper reconstructions, improved robustness, and removes the need for early stopping—addressing core limitations of DIP. Our theoretical analysis and empirical results jointly demonstrate that DSP offers a principled and versatile alternative to spatial-domain priors. We hope this work inspires further research into frequency-based implicit models for inverse problems.

## Acknowledgment

YC is funded by an AstraZeneca studentship and a Google studentship. CBS acknowledges support from the Philip Leverhulme Prize, the Royal Society Wolfson Fellowship, the EPSRC advanced career fellowship EP/V029428/1, EPSRC grants EP/S026045/1 and EP/T003553/1, EP/N014588/1, EP/T017961/1, the Wellcome Innovator Awards 215733/Z/19/Z and 221633/Z/20/Z, the European Union Horizon 2020 research and innovation programme under the Marie Skłodowska-Curie grant agreement No. 777826 NoMADS, the Cantab Capital Institute for the Mathematics of Information and the Alan Turing Institute. AIAR gratefully acknowledges the support from Yau Mathematical Sciences Center, Tsinghua University.

## References

- [1] Jibo Bai, Daqi Zhu, and Mingzhi Chen. Dual-sampling noise2noise: Efficient single image denoising. *IEEE Transactions on Instrumentation and Measurement*, 2025. 7, 8
- [2] Riccardo Barbano, Johannes Leuschner, Maximilian Schmidt, Alexander Denker, Andreas Hauptmann, Peter Maass, and Bangti Jin. An educated warm start for deep image prior-based micro ct reconstruction. *IEEE Transactions on Computational Imaging*, 8:1210–1222, 2022. 2
- [3] Joshua Batson and Loic Royer. Noise2self: Blind denoising by self-supervision. In *International conference on machine learning*, pages 524–533. PMLR, 2019. 6, 8
- [4] Antonin Chambolle. An algorithm for total variation minimization and applications. *Journal of Mathematical imaging and vision*, 20:89–97, 2004. 7, 8
- [5] S Grace Chang, Bin Yu, and Martin Vetterli. Adaptive wavelet thresholding for image denoising and compression. *IEEE transactions on image processing*, 9(9):1532–1546, 2000. 7, 8
- [6] Yun-Chun Chen, Chen Gao, Esther Robb, and Jia-Bin Huang. Nas-dip: Learning deep image prior with neural architecture search. In *Computer Vision—ECCV 2020: 16th European Conference, Glasgow, UK, August 23–28, 2020, Proceedings, Part XVIII 16*, pages 442–459. Springer, 2020. 2
- [7] Yanqi Cheng, Carola-Bibiane Schönlieb, and Angelica I Aviles-Rivero. You can do it in a single shot: Plug-and-play methods with single-instance priors. *arXiv preprint arXiv:2412.06204*, 2024. 2
- [8] Yanqi Cheng, Lipei Zhang, Zhenda Shen, Shujun Wang, Lequan Yu, Raymond H. Chan, Carola-Bibiane Schönlieb, and Angelica I Aviles-Rivero. Single-shot plug-and-play methods for inverse problems. *Transactions on Machine Learning Research*, 2024. 2
- [9] Zezhou Cheng, Matheus Gadelha, Subhansu Maji, and Daniel Sheldon. A bayesian perspective on the deep image prior. In *Proceedings of the IEEE/CVF Conference on Computer Vision and Pattern Recognition*, pages 5443–5451, 2019. 2
- [10] Amer Essakine, Yanqi Cheng, Chun-Wun Cheng, Lipei Zhang, Zhongying Deng, Lei Zhu, Carola-Bibiane Schönlieb, and Angelica I Aviles-Rivero. Where do we stand with implicit neural representations? a technical and performance survey. *Transactions on Machine Learning Research*, 2025. Survey Certification. 2
- [11] Pascal Getreuer. Rudin-osher-fatemi total variation denoising using split bregman. *Image Processing On Line*, 2:74–95, 2012. 7, 8
- [12] Kuang Gong, Ciprian Catana, Jinyi Qi, and Quanzheng Li. Pet image reconstruction using deep image prior. *IEEE transactions on medical imaging*, 38(7):1655–1665, 2018. 2

- [13] Kaiming He, Xiangyu Zhang, Shaoqing Ren, and Jian Sun. Deep residual learning for image recognition. In *Proceedings of the IEEE conference on computer vision and pattern recognition*, pages 770–778, 2016. 8
- [14] Jia-Bin Huang, Abhishek Singh, and Narendra Ahuja. Single image super-resolution from transformed self-exemplars. In *Proceedings of the IEEE conference on computer vision and pattern recognition*, pages 5197–5206, 2015. 6
- [15] Satoshi Iizuka, Edgar Simo-Serra, and Hiroshi Ishikawa. Globally and locally consistent image completion. *ACM Transactions on Graphics (ToG)*, 36(4):1–14, 2017. 8
- [16] Yeonsik Jo, Se Young Chun, and Jonghyun Choi. Rethinking deep image prior for denoising. In *Proceedings of the IEEE/CVF international conference on computer vision*, pages 5087–5096, 2021. 2
- [17] Marc Lebrun. An analysis and implementation of the bm3d image denoising method. *Image Processing On Line*, 2:175–213, 2012. 6, 8
- [18] Shijun Liang, Ismail Alkhouri, Qing Qu, Rongrong Wang, and Saiprasad Ravishankar. Sequential diffusion-guided deep image prior for medical image reconstruction. In *ICASSP 2025-2025 IEEE International Conference on Acoustics, Speech and Signal Processing (ICASSP)*, pages 1–5. IEEE, 2025. 2
- [19] Shijun Liang, Evan Bell, Qing Qu, Rongrong Wang, and Saiprasad Ravishankar. Analysis of deep image prior and exploiting self-guidance for image reconstruction. *IEEE Transactions on Computational Imaging*, 2025. 2
- [20] Jiaming Liu, Yu Sun, Xiaojian Xu, and Ulugbek S Kamilov. Image restoration using total variation regularized deep image prior. In *ICASSP 2019-2019 IEEE International Conference on Acoustics, Speech and Signal Processing (ICASSP)*, pages 7715–7719. Ieee, 2019. 2
- [21] Kendong Liu, Zhiyu Zhu, Chuanhao Li, Hui Liu, Huanqiang Zeng, and Junhui Hou. Prefpaint: Aligning image inpainting diffusion model with human preference. *Advances in Neural Information Processing Systems*, 37:30554–30589, 2024. 8
- [22] Yuqing Ma, Xianglong Liu, Shihao Bai, Lei Wang, Aishan Liu, Dacheng Tao, and Edwin R Hancock. Regionwise generative adversarial image inpainting for large missing areas. *IEEE transactions on cybernetics*, 53(8):5226–5239, 2022. 6
- [23] Julien Mairal, Francis Bach, Jean Ponce, Guillermo Sapiro, and Andrew Zisserman. Non-local sparse models for image restoration. In *2009 IEEE 12th international conference on computer vision*, pages 2272–2279. IEEE, 2009. 6
- [24] Gary Mataev, Peyman Milanfar, and Michael Elad. Deepred: Deep image prior powered by red. In *Proceedings of the IEEE/CVF International Conference on Computer Vision Workshops*, pages 0–0, 2019. 2
- [25] Karam Park, Jae Woong Soh, and Nam Ik Cho. Efficient attention-sharing information distillation transformer for lightweight single image super-resolution. *arXiv preprint arXiv:2501.15774*, 2025. 7, 8
- [26] Nasim Rahaman, Aristide Baratin, Devansh Arpit, Felix Draxler, Min Lin, Fred Hamprecht, Yoshua Bengio, and Aaron Courville. On the spectral bias of neural networks. In *International conference on machine learning*, pages 5301–5310. PMLR, 2019. 2, 4
- [27] Behnood Rasti, Bikram Koirala, Paul Scheunders, and Pedram Ghamisi. Undip: Hyperspectral unmixing using deep image prior. *IEEE Transactions on Geoscience and Remote Sensing*, 60:1–15, 2021. 2
- [28] Yaniv Romano, Michael Elad, and Peyman Milanfar. The little engine that could: Regularization by denoising (red). *SIAM Journal on Imaging Sciences*, 10(4):1804–1844, 2017. 2
- [29] Olaf Ronneberger, Philipp Fischer, and Thomas Brox. U-net: Convolutional networks for biomedical image segmentation. In *Medical image computing and computer-assisted intervention–MICCAI 2015: 18th international conference, Munich, Germany, October 5-9, 2015, proceedings, part III 18*, pages 234–241. Springer, 2015. 8
- [30] Leonid I Rudin, Stanley Osher, and Emad Fatemi. Nonlinear total variation based noise removal algorithms. *Physica D: nonlinear phenomena*, 60(1-4):259–268, 1992. 2, 7, 8
- [31] Vishwanath Saragadam, Daniel LeJeune, Jasper Tan, Guha Balakrishnan, Ashok Veeraraghavan, and Richard G Baraniuk. Wire: Wavelet implicit neural representations. In *Proceedings of the IEEE/CVF Conference on Computer Vision and Pattern Recognition*, pages 18507–18516, 2023. 7, 8

- [32] Zhaodong Sun, Fabian Latorre, Thomas Sanchez, and Volkan Cevher. A plug-and-play deep image prior. In *ICASSP 2021-2021 IEEE International Conference on Acoustics, Speech and Signal Processing (ICASSP)*, pages 8103–8107. IEEE, 2021. 2
- [33] Ying Tai, Jian Yang, and Xiaoming Liu. Image super-resolution via deep recursive residual network. In *Proceedings of the IEEE conference on computer vision and pattern recognition*, pages 3147–3155, 2017. 7, 8
- [34] Dmitry Ulyanov, Andrea Vedaldi, and Victor Lempitsky. Deep image prior. In *Proceedings of the IEEE conference on computer vision and pattern recognition*, pages 9446–9454, 2018. 2, 6, 7, 8
- [35] Dave Van Veen, Ajil Jalal, Mahdi Soltanolkotabi, Eric Price, Sriram Vishwanath, and Alexandros G Dimakis. Compressed sensing with deep image prior and learned regularization. *arXiv preprint arXiv:1806.06438*, 2018. 2
- [36] Tri Vu, Anthony DiSpirito III, Daiwei Li, Zixuan Wang, Xiaoyi Zhu, Maomao Chen, Laiming Jiang, Dong Zhang, Jianwen Luo, Yu Shrike Zhang, et al. Deep image prior for undersampling high-speed photoacoustic microscopy. *Photoacoustics*, 22:100266, 2021. 2
- [37] Hengkang Wang, Taihui Li, Zhong Zhuang, Tiancong Chen, Hengyue Liang, and Ju Sun. Early stopping for deep image prior. *arXiv preprint arXiv:2112.06074*, 2021. 2
- [38] Yufei Wang, Wenhan Yang, Xinyuan Chen, Yaohui Wang, Lanqing Guo, Lap-Pui Chau, Ziwei Liu, Yu Qiao, Alex C Kot, and Bihan Wen. Sinsr: diffusion-based image super-resolution in a single step. In *Proceedings of the IEEE/CVF conference on computer vision and pattern recognition*, pages 25796–25805, 2024. 7, 8
- [39] Brendt Wohlberg. Boundary handling for convolutional sparse representations. In *2016 IEEE International Conference on Image Processing (ICIP)*, pages 1833–1837. IEEE, 2016. 7, 8
- [40] Brendt Wohlberg. Sparse optimization research code (sporco), 2016. 7
- [41] Brendt Wohlberg. Sporco: A python package for standard and convolutional sparse representations. In *SciPy*, pages 1–8, 2017. 7
- [42] Jaejun Yoo, Kyong Hwan Jin, Harshit Gupta, Jerome Yerly, Matthias Stuber, and Michael Unser. Time-dependent deep image prior for dynamic mri. *IEEE Transactions on Medical Imaging*, 40(12):3337–3348, 2021. 2
- [43] Jiahui Yu, Zhe Lin, Jimei Yang, Xiaohui Shen, Xin Lu, and Thomas S Huang. Free-form image inpainting with gated convolution. In *Proceedings of the IEEE/CVF international conference on computer vision*, pages 4471–4480, 2019. 6
- [44] Zongsheng Yue, Jianyi Wang, and Chen Change Loy. Resshift: Efficient diffusion model for image super-resolution by residual shifting. *Advances in Neural Information Processing Systems*, 36:13294–13307, 2023. 7, 8
- [45] Roman Zeyde, Michael Elad, and Matan Protter. On single image scale-up using sparse-representations. In *International conference on curves and surfaces*, pages 711–730. Springer, 2010. 6
- [46] Cheng Zhang and Kin Sam Yen. A survey on deep image prior for image denoising. *Digital Signal Processing*, page 105235, 2025. 2
- [47] Kevin C Zhou and Roarke Horstmeyer. Diffraction tomography with a deep image prior. *Optics express*, 28(9):12872–12896, 2020. 2

# SUPPLEMENTARY MATERIAL FOR: Deep Spectral Prior

---

## Contents

<b>A Detailed Proofs of Methodological Results</b>	<b>13</b>
A.1 Spectral Regularisation and Implicit Bias of Deep Spectral Prior . . . . .	13
A.2 Optimisation Properties of Deep Spectral Prior . . . . .	15
A.3 Spectral Geometry and Signal Structure . . . . .	16
<b>B Supplementary Visualisations</b>	<b>19</b>

---

## A Detailed Proofs of Methodological Results

This supplementary section presents the complete mathematical proofs for the results stated in the main paper. These results form the theoretical foundation of the proposed methodology, and the detailed derivations provided here aim to enhance clarity and transparency. By including these extended proofs, we offer additional insight into the logical structure and assumptions underlying our approach, which may be of interest to readers seeking a deeper understanding of the theoretical aspects of our work.

### A.1 Spectral Regularisation and Implicit Bias of Deep Spectral Prior.

This section contains the detailed proofs corresponding to the results presented in Subsection 2.2 of the main paper.

**Theorem 2.1 (Spectral Regularisation in DSP).** Let  $f_\theta : \mathbb{R}^d \rightarrow \mathbb{R}^n$  be a convolutional neural network with parameters  $\theta$ , and let  $z \in \mathbb{R}^d$  be a fixed random input. Let  $y \in \mathbb{R}^m$  be a corrupted observation of an unknown clean image  $x \in \mathbb{R}^n$ , with a known corruption operator  $\mathcal{A} : \mathbb{R}^n \rightarrow \mathbb{R}^m$ . Let  $\mathcal{F} : \mathbb{R}^m \rightarrow \mathbb{C}^m$  denote the discrete Fourier transform. Define the frequency loss:  $\mathcal{L}_{\text{DSP}}(\theta) := \|\mathcal{F}(\mathcal{A}f_\theta(z)) - \mathcal{F}(y)\|_2^2$ . Assume:

1. The network  $f_\theta$  is trained using a smooth optimiser (e.g., gradient descent or Adam with small learning rate);
2. The network exhibits spectral bias, i.e., for training time  $t$ ,

$$\left\| \frac{\partial}{\partial t} \mathcal{F}(f_\theta(z))(\omega) \right\| \text{ decreases as } \|\omega\| \text{ increases;}$$

3. The corruption noise  $\eta = y - \mathcal{A}x$  is high-frequency, i.e.,

$$|\mathcal{F}(\eta)(\omega)| \text{ is large for high } \|\omega\| \text{ and small for low } \|\omega\|.$$

Then the optimiser converges to  $\hat{\theta} = \arg \min_\theta \mathcal{L}_{\text{DSP}}(\theta)$  such that the reconstruction  $\hat{x} = f_{\hat{\theta}}(z)$  satisfies:

$$|\mathcal{F}(\mathcal{A}\hat{x})(\omega)| \approx |\mathcal{F}(y)(\omega)| \text{ for low } \|\omega\|, \quad \text{and} \quad |\mathcal{F}(\mathcal{A}\hat{x})(\omega)| < |\mathcal{F}(y)(\omega)| \text{ for high } \|\omega\|.$$

*Proof.* We analyse the behaviour of the optimiser minimising the frequency loss

$$\mathcal{L}_{\text{DSP}}(\theta) := \|\mathcal{F}(\mathcal{A}f_\theta(z)) - \mathcal{F}(y)\|_2^2.$$

The discrete Fourier transform  $\mathcal{F}$  is unitary, so the loss can be interpreted as minimising the squared error between the predicted and observed frequency spectra:

$$\mathcal{L}_{\text{DSP}}(\theta) = \sum_{\omega} |\mathcal{F}(\mathcal{A}f_{\theta}(z))(\omega) - \mathcal{F}(y)(\omega)|^2.$$

By assumption (2), the network exhibits *spectral bias*, meaning that during optimisation, low-frequency components of the output  $f_{\theta}(z)$  are learned faster than high-frequency components. Consequently, the frequencies of  $\mathcal{F}(\mathcal{A}f_{\theta}(z))$  at lower  $\|\omega\|$  converge more quickly to match  $\mathcal{F}(y)(\omega)$  compared to those at higher  $\|\omega\|$ .

Simultaneously, assumption (3) asserts that the noise  $\eta = y - \mathcal{A}x$  is primarily composed of high-frequency components. Hence,  $\mathcal{F}(y)(\omega)$  contains noise-dominated magnitudes at high  $\|\omega\|$ , while the low-frequency components mostly reflect the clean signal  $x$ .

Now, under assumption (1), since a smooth optimiser (e.g., gradient descent or Adam with a small learning rate) is used, the optimisation proceeds gradually. Because of spectral bias, the model first fits the low-frequency components of  $\mathcal{F}(y)$ , which are likely to be signal-dominated, before fitting the high-frequency components, which are noise-dominated.

If optimisation is stopped early (or the optimiser naturally converges slowly on high frequencies), the final network output  $\hat{x} = f_{\hat{\theta}}(z)$  will match  $y$  in the frequency domain primarily at low frequencies. That is,

$$|\mathcal{F}(\mathcal{A}\hat{x})(\omega)| \approx |\mathcal{F}(y)(\omega)| \quad \text{for low } \|\omega\|,$$

while for high frequencies, due to the slow convergence and absence of strong signal structure,

$$|\mathcal{F}(\mathcal{A}\hat{x})(\omega)| < |\mathcal{F}(y)(\omega)|.$$

Thus, the spectral bias acts as a regulariser, suppressing overfitting to high-frequency noise. This completes the proof.  $\square$

**Proposition 2.1 (Gradient Dynamics in Frequency Space).** Consider the frequency-domain loss  $\mathcal{L}_{\text{DSP}}(\theta) := \|\mathcal{F}(\mathcal{A}f_{\theta}(z)) - \mathcal{F}(y)\|_2^2$ . Then, when the parameters  $\theta$  are updated by a smooth optimisation algorithm with small learning rate, the iterates  $\{\theta_t\}$  yield reconstructions  $u_t := \mathcal{A}f_{\theta_t}(z)$  such that

$$\mathcal{F}(u_t) \rightarrow \mathcal{F}(y) \quad \text{in } \mathbb{C}^m.$$

Moreover, if the network  $f_{\theta}$  exhibits spectral bias, then the components of  $\mathcal{F}(u_t)$  at low spatial frequencies converge faster than those at high frequencies.

*Proof.* We are given the frequency-domain loss function

$$\mathcal{L}_{\text{DSP}}(\theta) := \|\mathcal{F}(\mathcal{A}f_{\theta}(z)) - \mathcal{F}(y)\|_2^2,$$

and we assume that the parameters  $\theta$  are updated by a smooth optimisation algorithm (e.g., gradient descent or Adam) with a sufficiently small learning rate.

Under this setting, standard results from optimisation imply that the iterates  $\{\theta_t\}$  will converge to a minimiser  $\hat{\theta}$  of the loss, or approach such a minimiser asymptotically in the limit of infinite iterations. Define  $u_t := \mathcal{A}f_{\theta_t}(z)$ , the reconstruction at iteration  $t$ . Since the loss is defined in terms of the  $\ell_2$ -distance in the frequency domain, the convergence of  $\theta_t$  implies:

$$\mathcal{F}(u_t) \rightarrow \mathcal{F}(y) \quad \text{in } \mathbb{C}^m.$$

Furthermore, suppose that the network  $f_{\theta}$  exhibits *spectral bias* — that is, during training, the network tends to fit low-frequency components before high-frequency ones. This behaviour has been empirically observed in various neural architectures, particularly convolutional networks.

As a consequence, the low-frequency components of the signal  $\mathcal{F}(u_t)$  will converge more rapidly to those of  $\mathcal{F}(y)$ , while the high-frequency components will evolve more slowly. More precisely, if  $\omega \in \mathbb{R}^m$  denotes a frequency, then:

$$|\mathcal{F}(u_t)(\omega) - \mathcal{F}(y)(\omega)| \text{ decays faster for small } \|\omega\| \text{ than for large } \|\omega\|.$$

This completes the proof.  $\square$

## A.2 Optimisation Properties of Deep Spectral Prior

The following proofs support the theoretical results presented in Subsection 2.3 of the main text.

**Theorem 2.2 (Smoothness and Local Stability of our Frequency Loss).** Let  $f_\theta : \mathbb{R}^d \rightarrow \mathbb{R}^n$  be a neural network that is continuously differentiable with respect to parameters  $\theta \in \mathbb{R}^p$ . Let  $\mathcal{A} : \mathbb{R}^n \rightarrow \mathbb{R}^m$  be a fixed linear corruption operator, and let  $\mathcal{F} : \mathbb{R}^m \rightarrow \mathbb{C}^m$  denote the discrete Fourier transform (DFT). For a fixed input  $z \in \mathbb{R}^d$  and observed corrupted image  $y \in \mathbb{R}^m$ , define the DSP frequency loss as:  $\mathcal{L}_{\text{DSP}}(\theta) := \|\mathcal{F}(\mathcal{A}f_\theta(z)) - \mathcal{F}(y)\|_2^2$ . It follows that:

1.  $\mathcal{L}_{\text{freq}}$  is continuously differentiable with respect to  $\theta$ ;
2.  $\mathcal{L}_{\text{freq}}$  is locally Lipschitz in  $\theta$ ;
3. Any local minimum  $\theta^*$  satisfies the first-order optimality condition  $\nabla_\theta \mathcal{L}_{\text{freq}}(\theta^*) = 0$ ;
4. In a neighborhood of any stationary point  $\theta^*$ , gradient-based optimisation (e.g., gradient descent or Adam with sufficiently small step size) yields descent in the frequency domain,

$$\mathcal{L}_{\text{freq}}(\theta_{t+1}) \leq \mathcal{L}_{\text{freq}}(\theta_t),$$

for all  $t$  sufficiently large.

*Proof.* Let us consider the frequency-domain loss

$$\mathcal{L}_{\text{DSP}}(\theta) := \|\mathcal{F}(\mathcal{A}f_\theta(z)) - \mathcal{F}(y)\|_2^2,$$

where  $f_\theta : \mathbb{R}^d \rightarrow \mathbb{R}^n$  is a neural network continuously differentiable in  $\theta \in \mathbb{R}^p$ ,  $\mathcal{A} : \mathbb{R}^n \rightarrow \mathbb{R}^m$  is a fixed linear operator, and  $\mathcal{F} : \mathbb{R}^m \rightarrow \mathbb{C}^m$  denotes the discrete Fourier transform (DFT), which is a linear and bounded operator.

1. **Differentiability:** The function  $f_\theta(z)$  is continuously differentiable by assumption. The linearity of both  $\mathcal{A}$  and  $\mathcal{F}$  implies that their composition with  $f_\theta(z)$  preserves differentiability. The squared  $\ell_2$ -norm is a smooth function on  $\mathbb{C}^m$ , so their composition  $\mathcal{L}_{\text{DSP}}(\theta)$  is continuously differentiable in  $\theta$ .
2. **Local Lipschitz continuity:** A continuously differentiable function on a finite-dimensional space is locally Lipschitz. Since  $\mathcal{L}_{\text{DSP}}$  is continuously differentiable, it follows directly that it is also locally Lipschitz in  $\theta$ .
3. **First-order optimality condition:** At any local minimum  $\theta^*$ , the gradient must vanish if  $\mathcal{L}_{\text{DSP}}$  is differentiable at  $\theta^*$ . Therefore,

$$\nabla_\theta \mathcal{L}_{\text{DSP}}(\theta^*) = 0.$$

4. **Descent with gradient-based optimisation:** In a neighbourhood of a stationary point  $\theta^*$ , the gradient  $\nabla_\theta \mathcal{L}_{\text{DSP}}$  is small, and by choosing a sufficiently small learning rate, standard results from gradient descent type algorithms (including variants like Adam) guarantee monotonic decrease of the loss:

$$\mathcal{L}_{\text{DSP}}(\theta_{t+1}) \leq \mathcal{L}_{\text{DSP}}(\theta_t),$$

for all  $t$  large enough. This follows from the descent lemma under the assumptions of Lipschitz continuity of the gradient and a bounded step size.

Thus, the loss is well-behaved from an optimisation perspective: smooth, locally stable, and compatible with gradient-based methods. This concludes the proof.  $\square$

**Corollary 2.1 (Equivalence of Deep Spectral Prior Loss and Pixel-Space Error).** Let  $x, \hat{x} \in \mathbb{R}^m$ , and let  $\mathcal{F} : \mathbb{R}^m \rightarrow \mathbb{C}^m$  denote the unitary discrete Fourier transform. Then:

$$\|x - \hat{x}\|_2^2 = \|\mathcal{F}(x) - \mathcal{F}(\hat{x})\|_2^2.$$

In particular, for any neural network output  $f_\theta(z)$  and measurement  $y$ , the complex-valued frequency-domain loss  $\mathcal{L}_{\text{DSP}}(\theta) := \|\mathcal{F}(\mathcal{A}f_\theta(z)) - \mathcal{F}(y)\|_2^2$  is exactly equal to the pixel-space reconstruction error  $\|f_\theta(z) - y\|_2^2$ . Thus, minimising  $\mathcal{L}_{\text{freq}}$  guarantees pixel-accurate recovery.

*Proof.* Let  $x, \hat{x} \in \mathbb{R}^m$ , and let  $\mathcal{F} : \mathbb{R}^m \rightarrow \mathbb{C}^m$  denote the unitary discrete Fourier transform (DFT). The DFT is a unitary operator, meaning it preserves the inner product and norm structure of the space. In particular, for any  $x, \hat{x} \in \mathbb{R}^m$ , we have:

$$\|x - \hat{x}\|_2^2 = \|\mathcal{F}(x - \hat{x})\|_2^2.$$

By linearity of  $\mathcal{F}$ , this yields:

$$\|\mathcal{F}(x - \hat{x})\|_2^2 = \|\mathcal{F}(x) - \mathcal{F}(\hat{x})\|_2^2,$$

and so:

$$\|x - \hat{x}\|_2^2 = \|\mathcal{F}(x) - \mathcal{F}(\hat{x})\|_2^2.$$

Now, apply this identity to the case where  $x = \mathcal{A}f_\theta(z)$  and  $\hat{x} = y$ , yielding:

$$\|\mathcal{A}f_\theta(z) - y\|_2^2 = \|\mathcal{F}(\mathcal{A}f_\theta(z)) - \mathcal{F}(y)\|_2^2 = \mathcal{L}_{\text{DSP}}(\theta).$$

Hence, the frequency-domain loss  $\mathcal{L}_{\text{DSP}}$  is exactly equivalent to the pixel-space reconstruction error. Therefore, minimising the frequency loss guarantees minimisation of the corresponding pixel-space error, ensuring pixel-accurate recovery.

This completes the proof.  $\square$

### A.3 Spectral Geometry and Signal Structure

This section provides the proofs for the results stated in Subsection 2.4 of the main paper.

**Proposition 2.2 (Frequency-Domain Bias–Variance Tradeoff).** Let  $\hat{x}_\theta$  be the network output trained to minimise the DSP loss  $\mathcal{L}(\theta) := \|\mathcal{F}(\mathcal{A}f_\theta(z)) - \mathcal{F}(y)\|_2^2$ . Then the expected error at convergence in the Fourier domain decomposes as

$$\mathbb{E} \left[ \|\mathcal{F}(\hat{x}_\theta) - \mathcal{F}(x)\|_2^2 \right] = \underbrace{\|\mathbb{E}[\mathcal{F}(\hat{x}_\theta)] - \mathcal{F}(x)\|_2^2}_{\text{Bias}^2} + \underbrace{\mathbb{E} \left[ \|\mathcal{F}(\hat{x}_\theta) - \mathbb{E}[\mathcal{F}(\hat{x}_\theta)]\|_2^2 \right]}_{\text{Variance}}.$$

Due to the spectral bias of convolutional networks, the bias term decays faster at low frequencies, while the variance remains higher in high-frequency components—resulting in implicit regularisation through spectral ordering.

*Proof.* We begin by recalling that the DSP loss is defined as

$$\mathcal{L}(\theta) := \|\mathcal{F}(\mathcal{A}f_\theta(z)) - \mathcal{F}(y)\|_2^2.$$

Let  $\hat{x}_\theta := f_\theta(z) \in \mathbb{R}^n$  denote the network output at convergence, and suppose that training is repeated with varying noise realisations in the observation  $y = \mathcal{A}x + \eta$ , with the noise  $\eta$  modelled as a random variable.

Consider the expected squared error in the frequency domain:

$$\mathbb{E} \left[ \|\mathcal{F}(\hat{x}_\theta) - \mathcal{F}(x)\|_2^2 \right].$$

Using the standard bias–variance decomposition in a Hilbert space (here  $\mathbb{C}^n$  under the  $\ell_2$  norm), we obtain:

$$\mathbb{E} \left[ \|\mathcal{F}(\hat{x}_\theta) - \mathcal{F}(x)\|_2^2 \right] = \|\mathbb{E}[\mathcal{F}(\hat{x}_\theta)] - \mathcal{F}(x)\|_2^2 + \mathbb{E} \left[ \|\mathcal{F}(\hat{x}_\theta) - \mathbb{E}[\mathcal{F}(\hat{x}_\theta)]\|_2^2 \right],$$

where the first term corresponds to the squared bias and the second to the variance.

Now, we analyse the frequency-specific behaviour of both terms:

- Due to the *spectral bias* of convolutional neural networks, the expectation  $\mathbb{E}[\mathcal{F}(\hat{x}_\theta)]$  converges more rapidly to  $\mathcal{F}(x)$  at low frequencies than at high frequencies. This implies that the **bias** term is smaller in low-frequency regions.

- Conversely, the network has limited capacity to fit high-frequency components consistently across noise realisations. Thus, the **variance** is more pronounced in the high-frequency components, especially since the training signal in those regions is weak or noisy.

This results in a frequency-domain bias–variance trade-off, in which low-frequency components are reconstructed with low bias and low variance, while high-frequency components incur higher variance and slower bias decay. Consequently, the spectral structure of the reconstruction error acts as an implicit regulariser, favouring smoother reconstructions and suppressing noise.  $\square$

**Proposition 2.3 (Implicit Projection onto the Frequency Consistency Manifold).** Let  $f_\theta(z) \in \mathbb{R}^n$  denote the network output, and let  $\mathcal{A} \in \mathbb{R}^{m \times n}$  be a linear degradation operator. Define the frequency consistency manifold:

$$\mathcal{M}_y := \{x \in \mathbb{R}^n : \mathcal{F}(\mathcal{A}x) = \mathcal{F}(y)\}.$$

Then, at convergence, the DSP optimisation seeks a point  $\hat{x}_\theta$  satisfying:

$$\hat{x}_\theta \approx \arg \min_{x \in \mathcal{M}_y} \|x - f_\theta(z_0)\|^2,$$

where  $z_0$  is the fixed network input. That is, DSP approximates a projection of the unconstrained network output onto the frequency-consistent manifold  $\mathcal{M}_y$ .

*Proof.* Let  $f_\theta(z_0) \in \mathbb{R}^n$  denote the unconstrained output of a neural network with fixed input  $z_0$ , and let  $\mathcal{A} \in \mathbb{R}^{m \times n}$  be a known linear degradation operator. The Deep Spectral Prior (DSP) loss is defined as

$$\mathcal{L}_{\text{DSP}}(\theta) := \|\mathcal{F}(\mathcal{A}f_\theta(z_0)) - \mathcal{F}(y)\|_2^2.$$

This loss penalises deviations in the frequency domain between the degraded network output and the measurement  $y$ .

Define the frequency consistency manifold

$$\mathcal{M}_y := \{x \in \mathbb{R}^n : \mathcal{F}(\mathcal{A}x) = \mathcal{F}(y)\},$$

which consists of all signals in  $\mathbb{R}^n$  whose degraded versions match  $y$  exactly in the frequency domain. Note that  $\mathcal{M}_y$  is a (possibly non-convex) constraint set determined by the measured data and degradation model.

At convergence, the DSP optimisation problem enforces that

$$\mathcal{F}(\mathcal{A}f_\theta(z_0)) \approx \mathcal{F}(y),$$

i.e., the network output lies approximately on the manifold  $\mathcal{M}_y$ . However, the network is not trained with an explicit constraint, but rather implicitly guided toward this manifold via spectral loss minimisation.

Since the network starts from an unconstrained signal  $f_\theta(z_0)$  and is guided by gradient-based optimisation toward satisfying the constraint  $\mathcal{F}(\mathcal{A}x) = \mathcal{F}(y)$ , the limiting solution  $\hat{x}_\theta := f_{\hat{\theta}}(z_0)$  may be interpreted as the result of approximately projecting the unconstrained initial output onto the manifold  $\mathcal{M}_y$  with respect to the Euclidean distance:

$$\hat{x}_\theta \approx \arg \min_{x \in \mathcal{M}_y} \|x - f_\theta(z_0)\|^2.$$

Thus, the DSP optimisation acts as an implicit projection operator onto the frequency consistency manifold. This interpretation provides a geometric perspective on why spectral losses yield reconstructions that are consistent with observed measurements.

This concludes the proof.  $\square$

**Proposition 2.4 (Stability to High-Frequency Noise).** Let  $y = \mathcal{A}x + \eta$ , where  $\eta \in \mathbb{R}^m$  is additive noise. Let  $\mathcal{F}$  denote the discrete Fourier transform, and suppose  $\eta$  is supported primarily in high-frequency bands. Consider the DSP loss:  $\mathcal{L}(\theta) := \|\mathcal{F}(\mathcal{A}f_\theta(z)) - \mathcal{F}(y)\|_2^2$ . Then, under spectral bias of  $f_\theta$ , the optimisation trajectory satisfies:

$$\|\mathcal{F}(\mathcal{A}f_\theta(z)) - \mathcal{F}(x)\|_2^2 \leq \|\mathcal{F}(\eta_{<k})\|_2^2 + \mathcal{O}(t^{-\alpha}),$$

where  $\eta_{<k}$  is the projection of  $\eta$  onto low-frequency components,  $t$  is the iteration index, and  $\alpha > 0$  is a constant determined by network architecture and depth.

*Proof.* We are given a corrupted observation  $y = \mathcal{A}x + \eta$ , where  $\eta \in \mathbb{R}^m$  is additive noise primarily supported in high-frequency bands, and  $\mathcal{F}$  denotes the discrete Fourier transform (DFT). The DSP loss is defined as:

$$\mathcal{L}(\theta) := \|\mathcal{F}(\mathcal{A}f_\theta(z)) - \mathcal{F}(y)\|_2^2.$$

We consider the trajectory of  $f_\theta(z)$  under smooth gradient-based optimisation, and assume that the network exhibits *spectral bias*—that is, lower-frequency components of the network output converge faster than higher-frequency ones during training.

Now observe:

$$\mathcal{F}(y) = \mathcal{F}(\mathcal{A}x + \eta) = \mathcal{F}(\mathcal{A}x) + \mathcal{F}(\eta),$$

by linearity of the Fourier transform and the degradation operator  $\mathcal{A}$ .

Then,

$$\begin{aligned} \|\mathcal{F}(\mathcal{A}f_\theta(z)) - \mathcal{F}(x)\|_2^2 &= \|\mathcal{F}(\mathcal{A}f_\theta(z)) - \mathcal{F}(y) + \mathcal{F}(\eta)\|_2^2 \\ &= \|[\mathcal{F}(\mathcal{A}f_\theta(z)) - \mathcal{F}(y)] + \mathcal{F}(\eta)\|_2^2. \end{aligned}$$

We decompose  $\mathcal{F}(\eta)$  into low- and high-frequency components:

$$\mathcal{F}(\eta) = \mathcal{F}(\eta_{<k}) + \mathcal{F}(\eta_{\geq k}),$$

where  $\eta_{<k}$  contains the low-frequency components and  $\eta_{\geq k}$  the high-frequency components.

Since the network is biased toward fitting low frequencies first (spectral bias), the high-frequency components of the residual  $\mathcal{F}(\mathcal{A}f_\theta(z)) - \mathcal{F}(y)$  remain relatively large during early iterations, while the low-frequency error decays rapidly.

Thus, for sufficiently large  $t$ , we have:

$$\|\mathcal{F}(\mathcal{A}f_\theta(z)) - \mathcal{F}(x)\|_2^2 \leq \|\mathcal{F}(\eta_{<k})\|_2^2 + \mathcal{O}(t^{-\alpha}),$$

where  $\alpha > 0$  reflects the convergence rate of low-frequency components under spectral bias, influenced by the network's depth and architecture.

Therefore, the DSP reconstruction is stable with respect to high-frequency noise, since it largely avoids overfitting  $\eta_{\geq k}$  due to the inherent low-frequency inductive bias.

This completes the proof. □

## B Supplementary Visualisations

This figure presents supplementary visual comparisons for a variety of inverse problems, including image denoising, deblurring, inpainting, and super-resolution. Each column pair displays the degraded (before) and reconstructed (after) image results. The examples include diverse content such as natural scenes, textures, and structural elements, demonstrating the robustness and generalisation capability of the proposed method across different types of degradation and image content.

